

# Surfing, sweeping, and assembly of particles by a moving liquid crystal phase boundary

Tom Shneer,<sup>1</sup> Jocelyn Ochoa,<sup>2</sup> Alauna C. Wheeler,<sup>3</sup> Isabella C. Reyes,<sup>4</sup> Chaitanya Joshi,<sup>1</sup> Benjamin J. Stokes,<sup>4</sup> Linda S. Hirst,<sup>3</sup> and Timothy J. Atherton<sup>1,\*</sup>

<sup>1</sup>*Department of Physics & Astronomy, Tufts University, 574 Boston Ave, Medford, MA 02155*

<sup>2</sup>*Department of Chemistry & Biochemistry, University of California, Merced, 5200 N. Lake Merced, CA 95343*

<sup>3</sup>*Department of Physics, University of California, Merced, 5200 N. Lake Merced, CA 95343*

<sup>4</sup>*Department of Chemistry & Biochemistry, Santa Clara University, 500 El Camino Real, Santa Clara, CA 95053*

Non-equilibrium transport of particles embedded in a liquid crystal host can, by cooling through a phase transition, be exploited to create a remarkable variety of structures including shells, foams, and gels. Due to the complexity of the multicomponent system and protocol-dependent experimental results, the physical mechanisms behind structure selection remain only partially understood. Here we formulate a new model coupling LC physics to a Fokker-Planck equation as is commonly used in studies of transport. The resulting model allows us to draw an analogy between the LC-nanocomposite system and chemotaxis, enriching the space of possible target structures that could be produced. We study the model in one dimension both analytically and numerically to identify different parameter regimes where soliton-like pulses of particles “surf” the phase boundary or where the interface “sweeps” particles from one domain to another. We also consider an extended model that includes agglomeration of the particles and observe formation of periodic structures as a prototypical example of hierarchical self assembly. Results are compared with experimental observations of transport by isolated phase boundaries.

## I. INTRODUCTION

Nematic liquid crystal-nanoparticle (NLC-NP) composites are an attractive union of two very different materials: Submicron colloidal particles possess unique physical, chemical and optical properties due to their small size and high surface area to volume ratio. These particles, when dispersed in a host anisotropic NLC solvent, provide a spatially ordered, externally controllable, and optically active medium. Adjusting one or both components provides a great degree of control over macroscopic properties such as specific heat [1], shear and storage modulus [2–5], dielectric anisotropy, and elastic constants[6].

The liquid crystal component can also guide directed assembly of the colloidal particles[7]. When the system is cooled from a homogeneous initial state through the host’s nematic-isotropic (NI) phase transition, dispersed nano-[8] and even micron-scale[9] particles are observed to be transported by the moving NI phase boundary. The particles are typically coated with specially designed ligands to promote stability in the host phase and control aggregate formation [6, 10–12]. By adjusting experimental conditions, a number of morphologies can be produced with structure on length scales that are orders of magnitude larger than the constituent particles: solid hollow capsules which can be extracted from the host[8, 11, 13, 14], hierarchical structures formed by aggregation of these hollow capsules in liquid crystal [15], as well as networks and solid foams[8, 16–18]. Some structures can be formed reversibly and are stabilized by the host solvent[19–21], whereas structures can also be sta-

bilized by taking advantage of ligand-ligand interactions [10].

Exploiting the wide variety of morphologies and material properties possible with these materials may lead to applications in optics [22], device fabrication [23], medicine [24], cosmetics [25] and food science [26]. Nonetheless, an impediment to adopting and optimizing NLC-NP composites for particular applications is the lack of a fundamental understanding of what guides structure selection.

In this paper, we construct a phenomenological model of particle transport by a moving phase boundary and use our model to provide a unified understanding of phenomena observed in the formation of NLC-NP composites. We compare the model with experimental high speed video imaging of quantum dot transport near moving phase boundaries. A number of authors have previously drawn from the theory of dynamic critical phenomena [27] to model transport processes in LCs[19, 28–31]. In the critical phenomena framework, the density of particles and liquid crystal order parameter are described as continuous fields that evolve in time according to a coupled system of partial differential equations derived from a free energy.

Here we take a different approach, describing the phase transition by an Allen-Cahn equation and the particle transport through a Fokker-Planck equation. We also consider extensions to this model incorporating irreversible agglomeration of the particles. The resulting theories are closely related to the Keller-Segel model[32], providing an analogy between the formation of NLC-NP composites and chemotaxis. We study numerical solutions of the theory that predict periodic assembly of particles as observed experimentally [9, 33].

The paper is organized as follows: In Section II, we

\* timothy.atherton@tufts.edu

review prior experimental results that our model must predict; we then present our model in Section III and contrast it with prior approaches. The new formulation provides an analogy between nanoparticle transport and chemotaxis, which we discuss in Section III C. We present analytical and numerical results in Section IV, finding two regimes for particle transport including a “surfing” scenario where soliton-like perturbations are advected by the interface without disturbing the nanoparticle distribution and a “sweeping” regime where the interface partially or completely clears nanoparticles from the growing domain. These results are compared to experimental video imaging data.

We also demonstrate, in Section IV C, that if solidification is added into our model hierarchical structure formation naturally emerges. We draw conclusions in Section V.

## II. BACKGROUND

A number of experiments have characterized transport of particles during liquid crystal phase transitions[8, 17, 19, 20]. Micron-sized particles show transport of particles influenced by the nematic director with attraction to and trapping in isotropic domains [7], and that these effects could be strongly affected by the particles’ anchoring condition [34]. Such particles can be transported by spatially varying order parameters, either induced by temperature gradients[35] or by dopants[36]. With a specific ligand choice and particle size, logistic recovery of particles back into nematic domains following initial expulsion has also been observed[19].

Theoretical work on particle transport in liquid crystals has shown that particles can travel in either direction with respect to an order parameter or temperature gradient depending on a competition between thermophoretic and elastic forces[35]. Near an interface, the force on a particle is  $\propto dr$  with  $d$  the distance to the interface and  $r$  the particle size and that for a variety of anchoring conditions the free energy is reduced as the particle approaches the interface[37].

Structure selection is strongly affected by ligand choice, nanoparticle concentration, and cooling rate. The ligand affects the particles’ solubility, shifts the  $T_{NI}$  transition temperature and determines whether the final structure is stable; surprisingly the packing density of the particles is not correlated to the shell radius[11]. Dopants are also known to induce slowing down of the nematic-isotropic interface propagation speed[38].

Hollow structures were observed to form at all cooling rates and spherical shells were the only aggregates that form at very high cooling rates [8]. Different ligands lead to shells of different radius and thickness [11]. Slower cooling and increased nanoparticle concentration leads to larger shells[8]. Periodic aggregation has been observed by a number of authors[9, 19, 39] where the spacing and aggregate size are inversely related to the cooling rate.

Approximately periodic aggregation was observed in [14] with an ODA ligand.

Prior modelling of spherical shell formation includes simple scaling arguments, balancing the stress on the shell due to the phase boundary with that due to the nanoparticles. This predicts that the thickness of the shell is inversely proportional to its radius[11]. Ref. [40] models shell formation using Monte Carlo minimization of an effective free-energy functional including terms that account for nanoparticle-nanoparticle volume exclusion, the isotropic-nematic phase transition energy and nematic elasticity respectively. They find the shell thickness is set by a competition between the first two terms, with elasticity controlling the activation barrier for the transition. After formation, a continuum model with flexible boundaries predicts that the shells can be deformed by the local nematic and self-organize into chain. This was confirmed experimentally in Ref. [41].

Network and foam-like structures have also been created. Networks occur at slower cooling rates, while foams emerge as cooling rate is increased in [18]. Other authors find foam structures at intermediate cooling rates [8]. Foam cell size is inversely related to initial particle concentration [42]. At higher cooling rates, the networks can transition to a fern-like structure with smaller empty cells, higher density of cells, and thinner branches [17]. Mesogenic ligands intended to promote solubility result in a diffuse network with higher nanoparticle concentration at vertices of the network[14].

Some progress has been made on modelling higher order structures. Ref. [8] developed a Lebwohl-Lasher lattice model of the liquid crystal coupled to a Cahn-Hilliard model representing the nanoparticle phase separation, and observed segregation of particles into domain-like structures with the characteristic size of the domains varying inversely with the cooling rate. Following the critical phenomena approach of Hohenberg and Halperin[27], authors in ref. [31] formulate an effective free energy for the particle density and order parameter and solve the resulting dynamical equations numerically in two dimensions using finite differences. We shall discuss this approach in more detail in III B. Finally, formulating a model of spinodal decomposition in mixtures of a liquid crystal and colloidal particles, ref. [29] finds many morphologies including fibrous, cell-like or bicontinuous networks.

## III. MODEL

Our model describes the configuration of the system by two spatially varying and time dependent fields, the density of particles  $\rho(\mathbf{x}, t)$  and the scalar order parameter  $S(\mathbf{x}, t)$  of the host liquid crystal. In places where the system is isotropic,  $S = 0$ . We will assume that the NLC-NP composite is cooled uniformly with an instantaneous temperature  $T(t)$ .

Evolution of the liquid crystal order parameter is given

by the equation,

$$\beta \frac{\partial S}{\partial t} = \nabla \cdot \frac{\partial F}{\partial \nabla S} - \frac{\partial F}{\partial S}, \quad (1)$$

where  $F$  is the free energy of the system and  $\beta$  is a transport coefficient. We use the free energy,

$$F = \frac{1}{2}\alpha(\nabla S)^2 + \frac{3}{4}a_0\Delta TS^2 - \frac{1}{4}bS^3 + \frac{9}{16}cS^4, \quad (2)$$

where the first term is an elastic term with parameter  $\alpha$  that penalizes variation in  $S$  and the last three terms are the Landau expansion with associated coefficients  $a_0$ ,  $b$  and  $c$  that select a preferred value of  $S$ . The preferred bulk value  $S_0$  determined by minimizing the Landau terms is a function of  $\Delta T = T - T_0$  where  $T_0$  is the temperature below which the isotropic phase is no longer stable. Between  $0 < \Delta T < b^2/(27a_0c)$  both phases are stable but the nematic phase has lower energy; between  $b^2/(27a_0c) < \Delta T < b^2/(24a_0c)$  the isotropic phase has lower energy and for  $\Delta T > \Delta T_c = b^2/(24a_0c)$  only the isotropic phase is stable. Substituting Eq. (2) into (1) yields an Allen-Cahn-like equation,

$$\beta \frac{\partial S}{\partial t} = \alpha \nabla^2 S - \frac{3}{2}a_0\Delta TS + \frac{3}{4}bS^2 - \frac{9}{4}cS^3. \quad (3)$$

We describe the evolution of the particles using a Fokker-Planck equation,

$$\partial_t \rho = \nabla \cdot [D \nabla \rho - \mathbf{f}(S)\rho], \quad (4)$$

where  $D$  is the diffusion constant. The vector quantity  $\mathbf{f}(S)$  represents an external force that acts on the particles which we assume must depend on the phase field  $S$ . We may construct an expression for  $\mathbf{f}(S)$  from the order parameter  $S$  and its derivatives  $\nabla S$  etc and the simplest choice consistent with experimental studies of particle transport in LCs[36] is,

$$\mathbf{f}(S) = -\chi \nabla S, \quad (5)$$

where  $\chi$  is a parameter that characterizes the degree of forcing.

The form of Eq. (5) suggests an interpretation for  $S$ , in that it acts as an effective potential for the nanoparticles. Depending on the sign of  $\chi$ , the particles will either tend to be transported to the nematic domain ( $S > 0$ ) or to the isotropic domain ( $S = 0$ ). Close to a phase boundary, the particles experience a force and are pushed along. Far from a phase boundary the distribution of nanoparticles relaxes diffusely.

We now discuss a number of simplifying assumptions that we have made in formulating the above model. We assume that the particles are non-interacting, except for the diffusive behavior explicitly modeled. We consider only isotropic diffusion of the nanoparticles, because in the scenario considered here the particles largely remain in the isotropic phase and are strongly driven by advective forces at the interface. We neglect flow effects by using an equation of the form (1).

Another assumption is that the behavior of the LC is unaffected by the presence of nanoparticles since Eq. (3) does not depend on  $\rho$ . Such a coupling between the nanoparticle concentration and the phase behavior could emerge in a number of ways: The LC transition temperature itself has been theoretically predicted[43, 44] and experimentally shown[8, 19, 20] to be modified by the presence of nanoparticles depending on their radius. The interface velocity might be affected by the assembly of nanoparticles, as suggested in [18] and modeled in [44]. Further, in the critical phenomena formalism described below, inclusion of  $S$  in the dynamic equation for  $\rho$  implies that  $\rho$  should be included in the dynamical equation for  $S$ . While such couplings are likely to be important for determining the nucleation rate[17], they can be neglected if the nanoparticle concentration is very dilute and in any case do not appear to be essential to predict the assembly phenomena studied here. We similarly neglect possible temperature dependence of other quantities such as  $D$  and  $\chi$ , largely because we are interested in behavior close to the transition temperature. Finally, by considering a scalar order parameter only, we cannot capture phenomena such as LC defect formation and interactions with nanoparticles [45, 46].

### A. Nondimensionalization

We nondimensionalize Eq. (1) by introducing a timescale  $\tau$ , a lengthscale  $\xi$  and rearranging,

$$\frac{\partial S}{\partial t} = \alpha' \nabla^2 S - a'_0 \Delta TS + b' S^2 - c' S^3, \quad (6)$$

with new constants,

$$\alpha' = \frac{\alpha\tau}{\xi^2\beta}, \quad a'_0 = \frac{3}{2} \frac{a_0\tau}{\beta}, \quad b' = \frac{3}{4} \frac{b\tau}{\beta}, \quad c' = \frac{9}{4} \frac{c\tau}{\beta}.$$

We similarly nondimensionalize the Fokker-Planck equation,

$$\frac{\partial \rho}{\partial t} = \nabla \cdot [D' \nabla \rho + \chi' (\nabla S) \rho], \quad (7)$$

where,

$$D' = \frac{\tau D}{\xi^2}, \quad \chi' = \frac{\tau \chi}{\xi^2}. \quad (8)$$

We use values for the material 5CB  $a_0 = 0.087 \times 10^6 N/m^2/K$ ,  $b = 2.13 \times 10^6 N/m^2$ ,  $c = 1.73 \times 10^6 N/m^2$  and  $\alpha \sim 1 \times 10^{-11} N$ [47]. The transport coefficient  $\beta = \gamma_1/(9S_b^2)$  is related to the rotational viscosity  $\gamma_1 = \alpha_3 - \alpha_2 = 0.0777 \text{ Pa} \cdot s$  from Stewart[48] and is approximately constant with temperature[49].

We may conveniently choose a timescale  $\tau$  so that  $\beta/\tau = 10^6 N/m^2$  cancels the magnitude of the Landau coefficients, implying  $\tau \sim 10 \text{ ns}$ . We also choose  $\xi^2$  so that  $\alpha' = \frac{\alpha\tau}{\xi^2\beta} = 1$ , leading to  $\xi \sim 3 \text{ nm}$ . Having nondimensionalized the model, we will drop the primes henceforth and refer only to the dimensionless parameters.

## B. Comparison with the critical phenomena framework

As noted earlier, a number of authors have previously constructed models for particle transport drawing upon the theory of dynamic critical phenomena[19, 28–31]. To construct such a model, one begins with a free energy expressed as a function of relevant thermodynamic quantities, here  $S$  and  $\rho$ . The evolution of these fields is then described by dynamical equations derived from the free energy. The scalar order parameter evolves as we already described in (1), while the conserved particle density must evolve as follows,

$$\frac{\partial \rho}{\partial t} = \nabla^2 \left[ \frac{\partial f}{\partial \rho} - \nabla \cdot \frac{\partial f}{\partial \nabla \rho} \right]. \quad (9)$$

The combined evolution of a conserved quantity, the total number of particles, and a non-conserved quantity, the LC order, is referred to as ‘Model C’ in the classification of Hohenberg and Halperin[27].

Our model is closely related to, but distinct from, this framework. While the equation for the evolution of  $S$  is similar, the alternative formulation for  $\rho$  as a Fokker-Planck equation is more general because non-conservative forces, i.e. those that cannot be derived from a free energy, can be included. It also facilitates a rich connection to other fields of physics that describe transport through Fokker-Planck equations as we shall momentarily show.

## C. Analogy with chemotaxis

In this section we show that the model formulated above can be mapped onto the Keller-Segel model[32] of *chemotaxis*, a process by which the motion of autonomous agents, which could be entire organisms or individual cells, move in response to chemical cues. Their original paper considered the aggregation of slime molds, incorporating a feedback loop by which amoebae create reactants that react to produce a byproduct, acrasin, that serves to attract other amoebae.

Stated in a general form[50], the Keller-Segel model describes the co-evolution of a population of homogeneous agents with spatial distribution  $p$ ,

$$\frac{\partial p}{\partial t} = \nabla \cdot [\phi(p, q) \nabla p - \psi(p, q) \nabla p] + f(p, q), \quad (10)$$

together with the concentration of a chemical cue  $q$ ,

$$\frac{\partial q}{\partial t} = d \nabla^2 q + g(p, q) - h(p, q)q. \quad (11)$$

A number of quantities must be specified to complete the model:  $\phi(p, q)$  controls the agents’ diffusion,  $\psi(p, q)$  advection and  $f(p, q)$  reproduction while the functions  $g(p, q)$  and  $h(p, q)$  specify the dynamics of the cue.

To make the analogy between our model and the Keller-Segel explicit, we note that our density of nanoparticles  $\rho$  maps onto the density of agents  $p$ , while the scalar order parameter  $S$  maps onto the concentration of chemical cue  $q$ . We see that Eq. (10) parallels the form of (4). Looking at these equations term by term, we first note that the diffusion function  $\phi(p, q)$  must be set constant to map onto  $D$  in (4). The last term in Eq. (10) is also straightforward: since the number of particles is conserved,  $f(p, q)$  must be set to zero.

The advection term  $\psi(p, q) \nabla p$  in Eq. (10) amounts to a particular choice of force function in Eq. (4). The force function used in the K-S model is  $\propto \nabla q$ , motivated by assumption that the amoebae are “*sensitive to the relative acrasin gradient*” [32, 51]. Hence if  $\psi(p, q) \propto p$ , the advective term is equivalent to our choice of force function for the particle transport model Eq. (5), similarly proportional to  $\nabla S$ .

Now comparing the other pair of parallel equations Eq. (11) and (3), we see that by an appropriate choice of polynomials  $g(p, q)$  and  $h(p, q)$  the two equations can be made equivalent: the Laplacian term recovers curvature driven dynamics while terms arising from the Landau expansion amount to a particular choice of dynamics.

A great benefit of this analogy is that we may in future exploit the wealth of results about the Keller-Segel model, its extensions, and numerical techniques to solve it. Indeed, since Keller and Segel’s original paper, their model has been adapted and extended to study many other chemotactic processes, including hydrodynamic effects through the Keller-Segel-Navier-Stokes model, logistical growth models for reproduction, and modulations to the diffusion, to name a few [50, 52–54].

Of particular significance to the present work is that hierarchical self assembly structure formation is also observed in chemotactic systems. Endothelial cells, for example, have been shown to migrate under chemotactic influence to form vascular structures[55, 56] that remarkably resemble network structures observed in the LC-nanoparticle composites. Such a process can generate a wide range of cellular morphologies including clusters and networks[57]. Other examples of morphogenesis rely on chemotaxis-mediated pattern formation[58]. Despite the very different physics underlying the two classes of system, the new analogy presented here between phase-transition driven assembly and chemotactic assembly could provide a route to creating new biomimetic structures or even scaffolding new biological structures by exploiting results from the LC-nanocomposite system.

## IV. RESULTS

In this section, we obtain analytical and numerical solutions to our model Eqs. (6) and (7). For the purposes of this work, we shall focus on transport and assembly by a isolated moving interface. Isolated moving interfaces are observed in the initial stages of structure formation[8], as

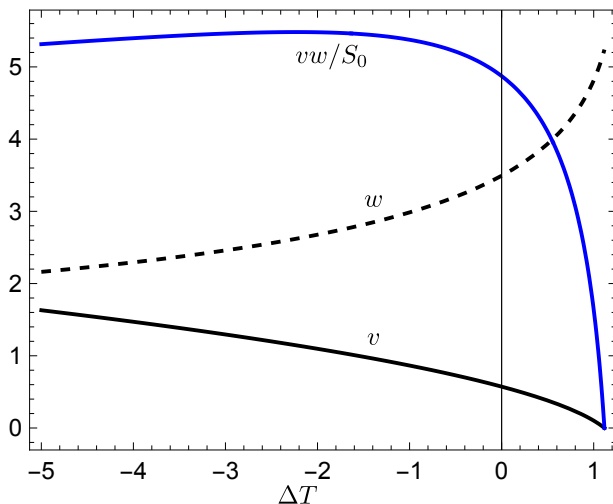


Figure 1. **Interface velocity  $v$  and width  $w$  as a function of temperature.** Also shown is the quantity  $vw/S_0$ , which determines the critical velocity.

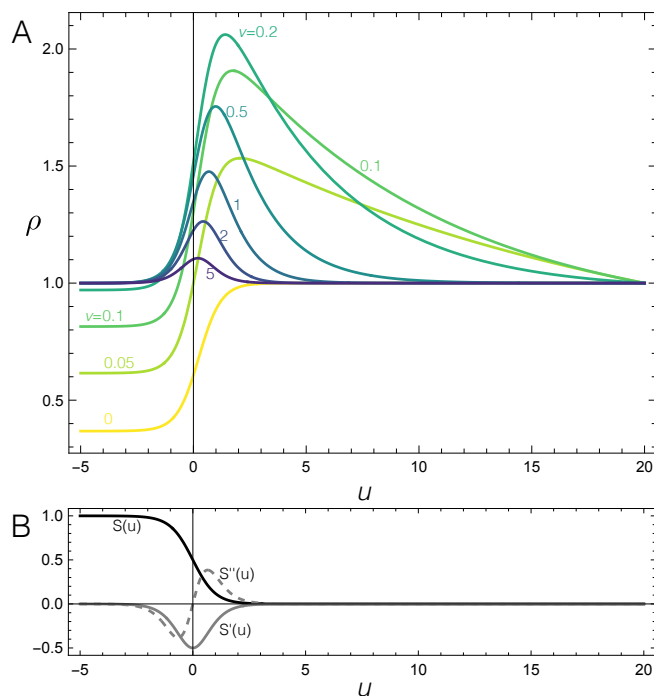


Figure 2. **Transition from ‘surfing’ to ‘sweeping’ in nanoparticle distributions guided by a moving interface.** **A** Distributions  $\rho(u)$  shown as a function of velocity with  $w = 1$  and parameters chosen so that  $v_c = 1$  and  $\frac{\chi S_0}{Dw^2} = 1$ . For low interface speeds  $v < v_c$ , nanoparticles are removed from the nematic domain; for  $v > v_c$ , a soliton like pulse of nanoparticles ‘surfs’ the phase boundary. **B** Profile of the corresponding nematic-isotropic interface  $S(u)$  and its derivatives. Calculations were performed on a domain  $[-L, L]$  with  $L = 20$  and only the right portion shown.

nematic domains are nucleated and grow upon cooling. Fluorescence images of the particle distribution exhibit a band of peak intensity adjacent to the phase boundary. Such a geometry is one dimensional and will be the subject of the remainder of this paper. In experimental geometries, domain growth is typically circular or spherical with a radius  $R(r)$  and hence the nematic-isotropic interface is curved. For simplicity, we shall neglect curvature which leads to a term  $\propto \frac{\alpha}{r} \frac{\partial S}{\partial r}$  in (6) arising from the Laplacian in polar coordinates; analogous terms arise in (7). Such a term is negligible for  $r \gg 1$  and if  $R \gg w$  where  $w$  is the width of the interface[59].

### A. Transport by a moving interface

To gain initial insight into the character of the solutions of our model Eqs. (6) and (7), we begin with an idealized scenario: A single interface between semi-infinite nematic and isotropic domains which moves at a constant velocity  $v$ , for which an analytical solution to (6) exists. In the comoving frame  $u = x - vt$ , Eq. (6) becomes,

$$\alpha \frac{d^2 S}{du^2} + v \frac{dS}{du} - a_0 \Delta T S + bS^2 - cS^3 = 0 \quad (12)$$

with a well-studied solution[60],

$$S = S_0 [1 - \tanh(u/w)]. \quad (13)$$

which represents an interface of width  $w$  about  $u = 0$  where the order parameter interpolates from the nematic phase  $S = S_0$  for  $u \ll 0$  to the isotropic phase  $S = 0$  for  $u \gg 0$ .

Inserting Eq. (13) into Eq. (12) and solving for  $v$  and  $w$  gives,

$$v = \frac{bS_0 - 3a_0 \Delta T}{\sqrt{2}\sqrt{bS_0 - a_0 \Delta T}}, w = \frac{2\sqrt{2\alpha}}{\sqrt{bS_0 - a_0 \Delta T}}, \quad (14)$$

At  $\Delta T_{eq}$ , the point at which the isotropic and nematic phase have equal energy, the interface velocity is zero. If the temperature is reduced, the interface width decreases, while the velocity of the interface increases as shown in Fig. 1.

Transforming the Fokker-Planck equation to the comoving frame yields,

$$\frac{\partial \rho}{\partial t} = D \frac{\partial^2 \rho}{\partial u^2} + \left( v + \chi \frac{\partial S}{\partial u} \right) \frac{\partial \rho}{\partial u} + \chi \frac{\partial^2 S}{\partial u^2} \rho. \quad (15)$$

We seek equilibrium solutions  $\frac{\partial \rho}{\partial t} = 0$ , and hence (15) becomes a second order homogenous ODE with spatially varying coefficients,

$$D \frac{d^2 \rho}{du^2} + A(u) \frac{d\rho}{du} + B(u) \frac{d^2 S}{du^2} \rho = 0, \quad (16)$$

where the coefficients are found by inserting the solution (13) into (16),

$$A(u) = \left( v - \frac{S_0\chi}{2w} \operatorname{sech}^2(u/w) \right), \quad (17)$$

$$B(u) = \frac{S_0\chi}{w^2} \operatorname{sech}^2(u/w) \tanh(u/w). \quad (18)$$

Since all parameters are positive,  $B(u)$  has a zero at  $u = 0$ , while  $A(u)$  has no zeros if  $v > \frac{S_0\chi}{2w}$  and two placed at  $u = \pm \operatorname{arccosh}\left(\sqrt{S_0\chi/2vw}\right)$  if  $0 < v < \frac{S_0\chi}{2w}$ . We therefore identify a critical velocity,

$$v_c = \frac{S_0\chi}{2w}, \quad (19)$$

and identify two important numbers,

$$\zeta = (v - v_c)/D, \quad \eta = \frac{\chi S_0}{Dw^2}, \quad (20)$$

that characterize the solution. The quantity  $vw/S_0$  is shown in Fig. 1; if  $vw/S_0 > \chi$  then  $\zeta$  is positive.

We now seek solutions consistent with the boundary conditions  $\rho(+L) = \rho_0$  and  $\rho'(-L) = 0$  for some  $L \gg w$ . Such a solution for  $v = 0$  is,

$$\rho = \rho_0 \exp\left(\frac{S_0\chi}{2D} [\tanh(u/w) - 1]\right), \quad (21)$$

which interpolates between a lower concentration in the  $u < 0$  nematic region and a higher concentration  $u > 0$  in the isotropic region. For finite  $v$ , we solve (16) numerically on a finite domain  $[-L, L]$  for various values of  $v$  and display the results in Fig. 2 together with the solution (13) and its derivatives. For larger values of  $v \gtrsim v_c$ , solutions resemble a soliton-like pulse around  $u = 0$  and the solution approaches  $\rho_0$  on the left hand boundary. As  $v$  is reduced the pulse becomes larger and increasingly asymmetric. Decreasing  $v$  further, around  $v \lesssim \frac{S_0\chi}{2L}$  the solution becomes affected by the right hand boundary condition and gradually deforms to agree with the  $v = 0$  solution. We therefore identify two regimes: a ‘‘surfing’’ regime where a pulse of particles is advected by the interface with the background undisturbed at  $v \gtrsim v_c$  and a ‘‘sweeping’’ regime  $0 \leq v \ll v_c$  whereby the interface partially or completely clears the nematic domain.

We also observe that the width of the particle distribution can be much greater than the width of the phase boundary as is consistent with experiments. For  $u \gg 0$ , the coefficients in Eq. (16) approach constant values  $A(u) \rightarrow v/D$  and  $B(u) \rightarrow 0$ ; hence the leading edge of the solution is of the form,

$$\rho \sim \exp(-uw/D), \quad (22)$$

and we identify a characteristic decay length  $\lambda = D/v$ .

The semi-infinite geometry considered in this section is sufficiently tractable analytically to enable us to identify qualitative features of particle distributions driven

by a moving interface. However, in some of the experiments described previously in Section II the temperature is changing with time. Hence, because the interface velocity  $v$ , the domain width  $w$ , and the order parameter  $S_0$  are all functions of temperature as discussed above in Section III, these quantities are all potentially functions of time as well as the system is cooled.

## B. Transport by a growing domain

The geometry considered in the preceding section, semi-infinite nematic and isotropic domains, is quite different from the experimental situation where a spatially uniform particle distribution that is disrupted by the nucleation of a nematic domain. We therefore turn to a more realistic scenario by modeling the behavior of  $S$  and  $\rho$  in the rest frame with an initial nematic domain seeded around  $x = 0$  at  $t = 0$ ,

$$S(x, 0) = S_0 \exp\left[-\left(\frac{x}{w_0}\right)^2 / 2\right], \quad (23)$$

where we choose values of  $S_0$  and  $w_0$  from (??) and (14) consistent with an initial temperature  $\Delta T$  and use material parameters given in subsection (III A). The initial condition on  $\rho$  is a constant  $\rho = \rho_0$ . We solve Eqs. (6) and (7) in *Mathematica* using the Method of Lines on a domain  $x \in [-L, L]$  and for  $t \in [0, T_0]$  with periodic boundary conditions. We choose  $L = 200$  and  $t = 200$  corresponding to a physical domain of  $\sim 1.2\mu\text{m}$  and a time of  $\sim 2\mu\text{s}$ .

We first study solutions at a fixed temperature and choose  $\Delta T = 0.2$ , which is in the region where both nematic and isotropic phase are stable, but with the nematic phase energetically favored. We examined solutions for other temperatures  $\Delta T < \Delta T_c$ , the limit of stability of the nematic phase, and find similar results.

In Fig. 3A, we display the spatial and temporal evolution of  $S$  as a *kymograph* as might be conveniently extracted from microscopy data; note only one half  $x > 0$  of the solution is shown. The nematic domain grows into the surrounding isotropic phase at constant velocity, as expected at fixed temperature. Corresponding kymographs for  $\rho$  are displayed in Fig. 3B and C as a function of the physically intuitive experimental parameters  $D$  and  $\chi$ . Variation of these parameters could be achieved, for example, by adjusting the particle size to change the diffusion constant or the ligand coating the nanoparticles to change  $\chi$  as was suggested in [8].

Kymographs showing the effect of varying  $\chi$  with fixed  $D = 5$  are shown in 3B, while in Fig. 3C we fix  $\chi = 200$  and vary  $D$ . For large  $\chi$ , the nanoparticle distribution is rapidly depleted from the nematic phase, forms a concentrated peak in the isotropic domain near the phase boundary and moves with it as the nematic grows into the isotropic. Such assembly and advective transport by the phase boundary has been observed experimentally[17].

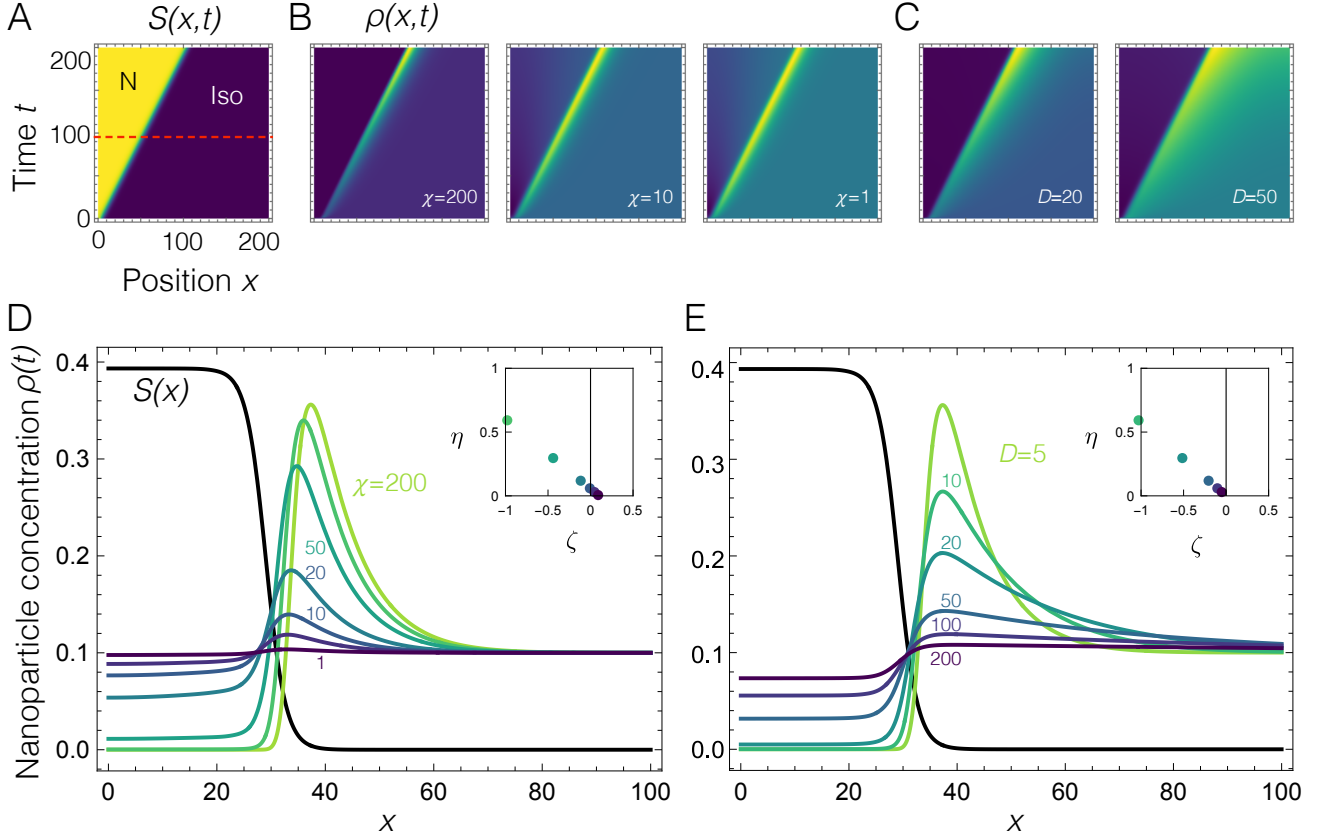


Figure 3. **Effect of varying forcing and diffusion constants.** **A** Kymograph of growing nematic domain with order parameter  $S(x, t)$  at fixed temperature  $\Delta T = 0.2$ . Red dashed line indicates the cross section visualized in D, E. **B** Corresponding particle distribution  $\rho(x, t)$  kymographs for  $D = 5$  and  $\chi = 200, 10, 1$ . **C** Particle distributions fixing  $\chi = 200$  and  $D = 20, 50$ . **D** Snapshots at  $t = 100$  of the interface  $S(x)$  (black line) and particle distribution  $\rho(x)$  (color lines) for  $D = 5$  and varying  $\chi$ . **E** Snapshots at  $t = 100$  for  $\chi = 200$  with varying  $D$ . *Insets:* Corresponding parameters  $\zeta, \eta$  for  $D, \chi$ . All solutions were solved on a domain  $[-L, L]$  with  $L = 200$ ; only the  $x > 0$  region is plotted.

Snapshots of particle distributions at a single moment in time, but with varying  $\chi$  and  $D$  are shown in Fig. 3E, F. In Fig. 3D, we vary  $\chi$  with  $D = 5$  while in Fig. 3E  $\chi = 200$  and  $D$  is varied. In the insets of each figure we show corresponding values of  $\zeta = (v - v_c)/D$  and  $\eta = \chi S_0/(Dw^2)$ . As predicted from the idealized model in the previous section, we see complete clearing of the nematic domain for  $\zeta \ll 0$ , the “sweeping” regime, which is the case for large  $\chi$  or small  $D$ . As  $\zeta$  approaches 0, which happens if  $\chi$  is sufficiently small or  $D$  sufficiently large, incomplete clearing of the nematic domain occurs, a result that has also been observed experimentally[19]. Also in agreement with our analysis of the single interface model, the width of the distribution is proportional to  $D$  and not affected by  $\chi$ . Both parameters affect the overall shape, especially the skewness, of the distribution.

Finally, we consider a reciprocal scenario where an isotropic domain grows into a nematic domain on heating. Such a situation obviously occurs only if the temperature is in the coexistence region. As an illustration, we perform simulations starting from an initial nucleated isotropic configuration  $S = S_0 [1 - \exp(-x^2/2w_0^2)]$

at  $\delta T = 10^{-4}$  just below  $\Delta T_c = b^2/24a_0c$  ( $\approx 1.25598$  with the Landau coefficients used) to maximize the interface velocity. The corresponding order parameter distribution is shown in Fig. 4A. In this situation, if the sign of  $\chi$  is also reversed, particles are driven into the nematic domain from the isotropic as shown in Fig. 4B and experimentally reported in [20]. A similar surfing/sweeping transition occurs as a function of  $\chi$  as shown through the snapshots of  $\rho$  at a single timepoint in Fig. 4C.

Hence, by choosing suitable values of the parameters, our model can account for and unites multiple observed transport scenarios by moving nematic-isotropic interfaces.

### C. Solidification

In this section, we create an illustrative example of hierarchical assembly by constructing an extension of the model developed in Section III that includes solidification i.e. the irreversible assembly of the particles. Experimentally, reversible assembly has been observed [1, 19];

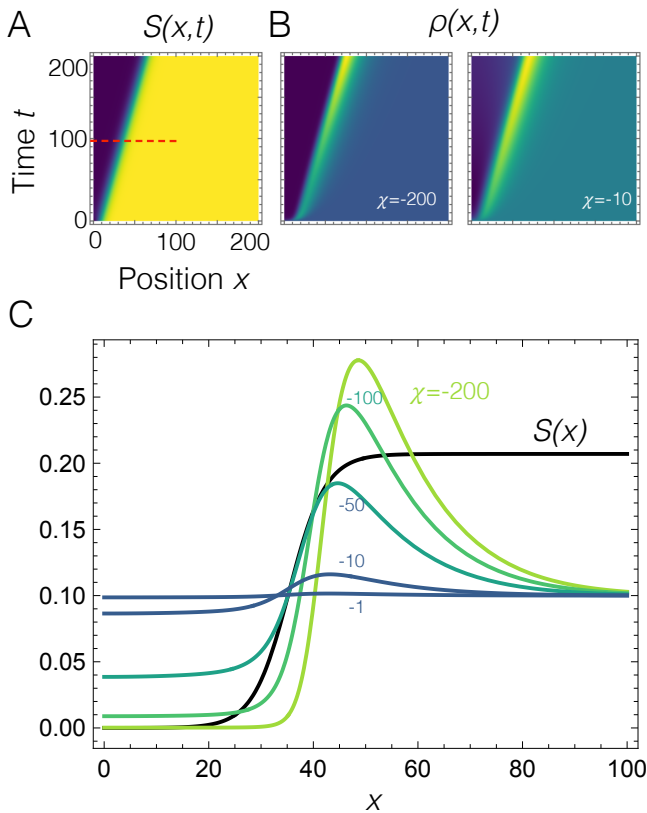


Figure 4. **Reciprocal scenario where nanoparticles are guided by a growing isotropic domain.** **A** Kymograph with order parameter  $S(x, t)$  at fixed temperature  $\Delta T = \Delta T_c - 10^{-4}$ . Red dashed line indicates the cross section visualized in **C**. **B** Corresponding particle distribution  $\rho(x, t)$  kymographs for  $D = 5$  and  $\chi = -200, -10$ . **C** Snapshots at  $t = 100$  of the interface  $S(x)$  (black line) and particle distribution  $\rho(x)$  (color lines) for  $D = 5$  and varying  $\chi$ . All solutions were solved on a domain  $[-L, L]$  with  $L = 200$ ; only a subinterval of the domain is shown for clarity.

here we focus on modelling situations where the assembly is irreversible [8, 13], at least on the timescales of the experiment. We assume that such assembly occurs on a timescale much shorter than it takes for particles to move a diffusion length.

To do so we introduce a new field  $\nu(x, t)$  that describes the distribution of particles that are no longer mobile. Particles are added to the assembly if the local particle density  $\rho + \nu$  exceeds a critical density  $\rho_*$ , which is achieved by a rate function,

$$R(\rho, \nu) = \rho \Gamma H(\rho + \nu - \rho_*) \quad (24)$$

where  $\Gamma$  is the overall rate of the reaction and  $H(z)$  is the Heaviside step function. For numerical conditioning, we use a continuous approximation of  $H(z)$ ,

$$H(z) \sim [1 - \exp(-kz)]^{-1}, \quad (25)$$

with a finite value  $k \gg 1$ .

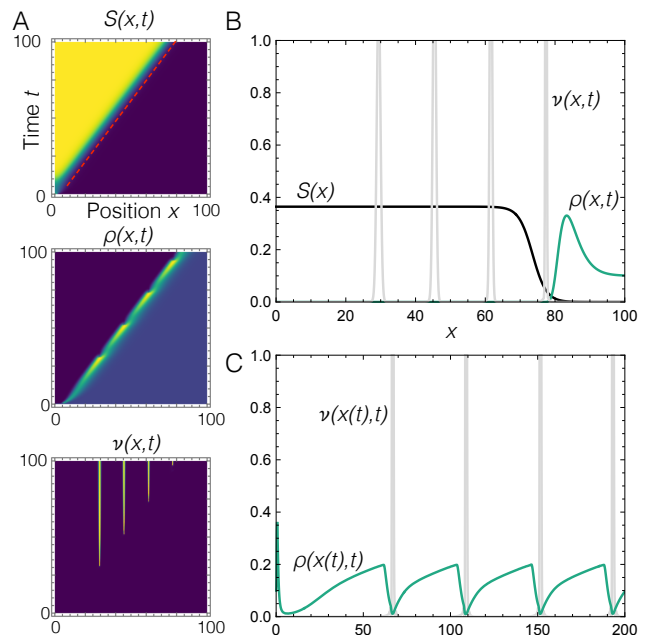


Figure 5. **Hierarchical assembly due to solidification.** **A** Kymographs of assembly process showing growing nematic domain with order parameter  $S(x, t)$ , mobile particle distribution  $\rho(x, t)$  and solid particle distribution  $\nu(x, t)$ . Red dashed line indicates the cross section visualized in **C**. **B** Snapshot at  $t = 100$  of the system showing periodically assembled bands. **C** Cross section of  $\rho$  and  $\nu$  along a contour  $x = 4 + vt$  showing periodic aggregation and solidification. Solution was evaluated on a domain  $[-L, L]$  with  $L = 200$ ; only a subinterval of the domain is shown for clarity.

The Fokker-Planck equation must be modified to include loss of particles to the solid,

$$\frac{\partial \rho}{\partial t} = \nabla \cdot [D \nabla \rho + \chi (\nabla S) \rho] - R(\rho, \nu), \quad (26)$$

and a new equation for  $\nu$ , the immobile particle density, introduced,

$$\frac{\partial \nu}{\partial t} = \epsilon \nabla^2 \nu + R(\rho, \nu), \quad (27)$$

The first term in (27) promotes relaxation of the solid and is necessary for numerical stability of the overall system (6), (7) and (27). Here, we use a small value for  $\epsilon$  to imply very slow relaxation.

In Fig. 5A we display kymographs showing the results of a typical simulation. We choose  $\chi$  and  $D$  so that the simulation is deep in the “sweeping” regime whereby particles are completely cleared from the nematic domain by the interface and fix temperature so that the interface width and velocity are constant. As the nematic domain grows, particles slowly accumulate ahead of it, and eventually exceed the critical density. At this point, the excess particles solidify in a narrow region, returning



$\rho$  to lower than its critical value; the process is therefore reset and repeats as the interface continues to proceed. On the kymograph for  $\nu$ , as well as a snapshot of the solution at  $t = T_0$ , Fig. 5B, we see the narrow regularly spaced bands of solid. The repeated process of accumulation of  $\rho$  and solidification is more clearly visible on a plot, Fig. 5C, of  $\rho$  and  $\nu$  at a single co-moving point  $x = x_0 + vt$  as a function of time.

#### D. Comparison with experiment

To test the predictions of the model, we prepared and imaged an experimental realization of nanoparticle transport guided by a nematic-isotropic phase transition as follows: We prepared a nanocomposite mixture following our reported protocol [8] where a 7.6 mg/mL toluene solution of CdSe/ZnS quantum dots coated with L1 ligand[10, 61] is dispersed in 5CB to yield a 0.75% (w/w) quantum dot solution in 5CB after toluene removal. This mixture was kept in an incubator at 50 °C, ensuring that the liquid crystal host remained in the isotropic phase prior to the controlled phase transition. Inside the incubator, 2.0  $\mu$ L of the nanocomposite mixture was pipetted onto a clean glass microscope slide and covered with a cover glass; A Kapton film spacer was used to ensure a liquid crystal film thickness of 25  $\mu$ m. The glass slide was sealed with UV glue and then removed from the incubator and quickly transferred to a temperature control stage (Linkam TMS94 & LTS 350, United Kingdom) held at 45 °C. To record videos of quantum dot distribution through the phase transition, the stage temperature was then decreased at a rate of 1°C per minute with aid of an in-house designed liquid nitrogen cooled air system. The phase transition was recorded using a Leica DM2500 LED fluorescence microscope, I3 fluorescence filter cube, and Phantom camera VEO 410L. Videos were recorded at various frame rates (24-200 frames per second) using either a 20X or 40X magnification objective lens.

A sequence of snapshots at different time points for a cropped region of interest from a representative video are displayed in Fig. 6A; the corresponding movie is provided as Supplementary Information. In this example, two relatively isolated domains are observed to nucleate and grow over a timescale of several seconds. A corona-like intensity maximum is observed around the growing domains, as was seen in [8]. A slice through the image stack going through the horizontal centerline of the domains is displayed as an  $(x, t)$  kymograph in Fig. 6B, showing the growth and movement of the particle corona as the domains grow. While the domain on the right nucleates slightly earlier, the growth and evolution of these two domains (and many others from other regions of interest) are very similar. Selected intensity profiles at highlighted time points are then shown in Fig. 6C; these have been averaged over 5 adjacent frames to improve the signal to noise ratio.

The time resolved intensity profiles show partial sweeping of nanoparticle concentration from the growing nematic domain, with a characteristic peak that grows and is advected along with the domain boundary. The shape of the peak strongly resembles that observed in our model, and hence we display snapshots from a simulation in Fig. 6D. To create these, we used Landau parameters for 5CB as described in subsection III A and used  $\Delta T = 0.1$  estimated from the observed timescale of the growth together with the known cooling rate. We adjusted  $\chi = 4$  and  $D = 0.6$  to approximately match the shape of the traces. Other choices of parameters are possible to reproduce the data, and careful independent measurements of the viscosity and/or diffusion constant would be needed to find a unique fit. Nonetheless, the shape, behavior and growth of the nanoparticle concentration predicted by the model is certainly observed in this data. Surprisingly, though, the interface velocity does not increase with time, as would be expected from the Landau model, but rather decreases. This could be due to intradomain interactions, or because the nanoparticle concentration strongly affects the transition temperature of the composite in the vicinity of the phase boundary and hence slows down the interface.

#### V. CONCLUSIONS

In this work, we have developed a model of particle transport by a moving phase boundary that couples an Allen-Cahn like equation arising from the dynamics of the nematic order parameter to a Fokker-Planck equation describing particle transport. Our model is related to, but departs from, the ‘Model C’ approach previously used to describe from the framework of critical phenomena. Formulating particle transport using the Fokker-Planck approach allows for forces that cannot be expressed as derivatives of a free energy, and also enables us to connect with the vast literature on stochastic transport that leverages this framework. As an illustration, we draw a new correspondence between our model and the Keller-Segel model of chemotaxis for living systems. This analogy suggests a number of new possible structures that might be created by the LC system, and offers the possibility of using advanced numerical techniques developed to solve such equations.

As an illustration of our model, we consider particle transport by an isolated phase boundary as is visible in the early stages of structure formation. By performing a careful analysis of this restricted scenario here, we shed new light on possible mechanisms guiding assembly of more complex structures, such as the gels, shells and foams experimentally observed. With one model, we reproduce numerous disparate experimental results including a transition between ‘sweeping’ particles from a growing nematic domain and soliton-like groups of particles ‘surfing’ the interface. The interface velocity, width and order parameter, which are all temperature dependent

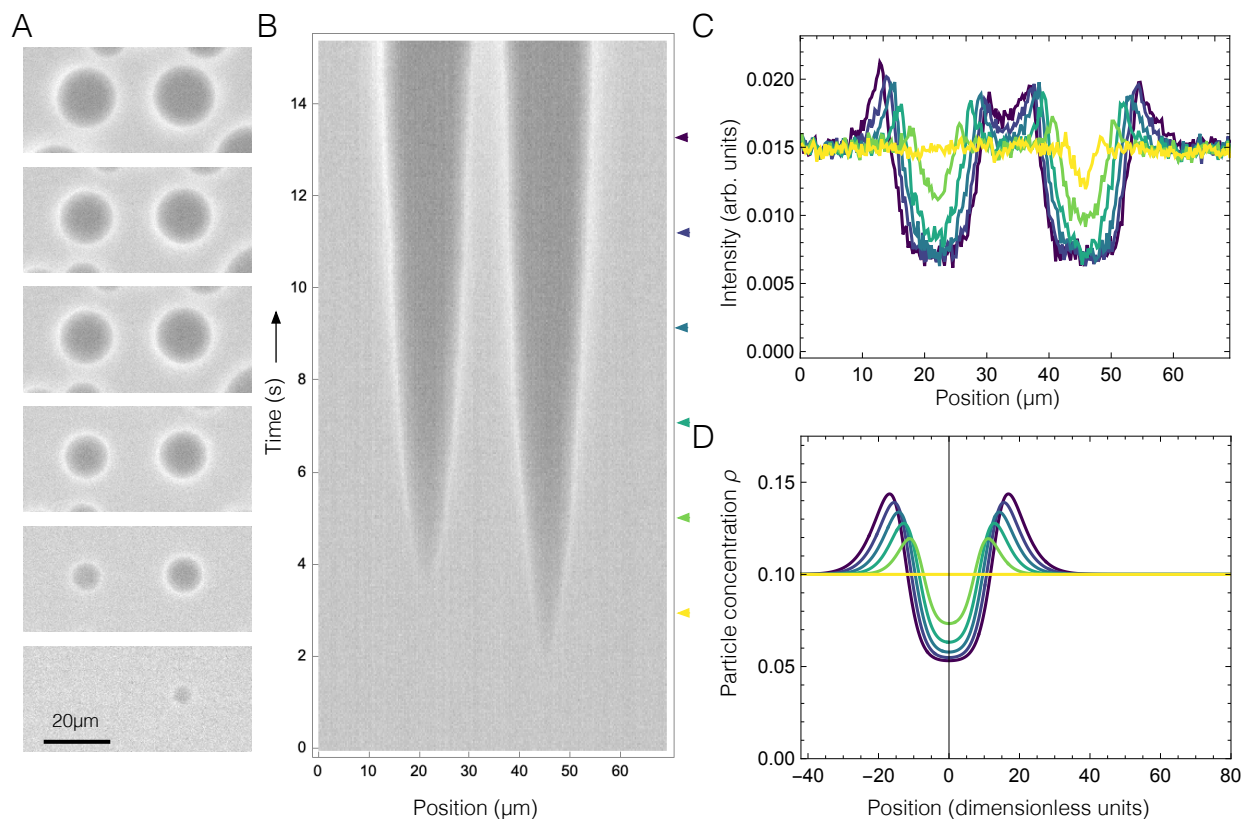


Figure 6. **Fluorescence microscope imaging of nanoparticle concentration during nematic domain nucleation and growth events.** **A** Snapshots of two relatively isolated domains at different timepoints. **B** Kymograph produced by slicing along the center of the domains. Arrows indicate time points shown in panels A and C. **C** Selected intensity traces at depicted time points. **D** Modelled evolution of the nanoparticle distribution.

quantities, play a key role in determining which regime the system is in.

By incorporating the possibility of solidification once a critical density is reached, we are able to produce regularly-spaced solid deposits, a one dimensional version of the hierarchical structures observed and with features on lengthscales far greater than the nanoparticle size or the interface width. In future work, we will apply this model to higher dimensional geometries to resolve the many outstanding questions about structure selection.

## ACKNOWLEDGMENTS

*TS and TJA designed the theoretical model and performed numerical simulations with input from CJ. JO, AW and LSH designed the experimental realization. ICR and BJS provided ligand L1. JO and TJA analyzed the data. All authors contributed to prepare the manuscript. This material is based upon work supported by the National Science Foundation under Grant No. DMR-2104575.*

- 
- [1] D. Vollmer, G. Hinze, B. Ullrich, W. C. K. Poon, M. E. Cates, and A. B. Schofield, *Langmuir* **21**, 4921–4930 (2005).
- [2] S. Kumar, G. Singh, and P. Thareja, *Journal of Molecular Liquids* **314**, 113623 (2020).
- [3] P. G. Petrov and E. M. Terentjev, *Langmuir* **17**, 2942–2949 (2001).
- [4] S. P. Meeker, W. C. K. Poon, J. Crain, and E. M. Terentjev, *Physical Review E* **61**, R6083–R6086 (2000).
- [5] V. Anderson and E. Terentjev, *The European Physical Journal E* **4**, 21–28 (2001).
- [6] H. Qi, B. Kinkead, V. M. Marx, H. R. Zhang, and T. Hegmann, *ChemPhysChem* **10**, 1211 (2009).
- [7] O. D. Lavrentovich, *Soft Matter* **10**, 1264 (2013), 1311.6846.
- [8] S. T. Riahinasab, A. Keshavarz, C. N. Melton, A. Elbaradei, G. I. Warren, R. L. Selinger, B. J. Stokes, and L. S. Hirst, *Nature Communications* **10**, 10.1038/s41467-019-08702-3 (2019).
- [9] J. L. West, A. Glushchenko, G. Liao, Y. Reznikov, D. Andrienko, and M. P. Allen, *Phys. Rev. E* **66**, 012702 (2002).
- [10] A. Keshavarz, S. T. Riahinasab, L. S. Hirst, and B. J. Stokes, *ACS Applied Nano Materials* **2**, 2542–2547 (2019).

- [11] R. Brisbin, M. Bartolo, M. Leville, A. K. Rajan, B. Jahan, K. E. McCloskey, A. Gopinathan, S. Ghosh, and R. Baxter, *Scientific Reports* **12**, 844 (2022).
- [12] E. R. Soulé, J. Milette, L. Reven, and A. D. Rey, *Soft Matter* **8**, 2860 (2012).
- [13] A. L. Rodarte, B. H. Cao, H. Panesar, R. J. Pandolfi, M. Quint, L. Edwards, S. Ghosh, J. E. Hein, and L. S. Hirst, *Soft Matter* **11**, 1701–1707 (2015).
- [14] A. L. Rodarte, Z. S. Nuno, B. H. Cao, R. J. Pandolfi, M. T. Quint, S. Ghosh, J. E. Hein, and L. S. Hirst, *ChemPhysChem* **15**, 1413–1421 (2014).
- [15] D. G. Sudha, J. Ochoa, and L. S. Hirst, *Soft Matter* **17**, 7532–7540 (2021).
- [16] H. Diestra-Cruz, E. Bukusoglu, N. L. Abbott, and A. Acevedo, *ACS Applied Materials & Interfaces* **7**, 7153 (2015).
- [17] L. Zou, J.-Y. Hwang, and C. Kim, *Physical Review E* **88**, 042505 (2013).
- [18] J. Cleaver and W. C. Poon, *Journal of Physics: Condensed Matter* **16**, 10.1088/0953-8984/16/19/003 (2004).
- [19] N. M. Fhionlaoich, S. Schrettl, N. Tito, Y. Yang, N. Malavika, L. Serrano, K. Harkness, P. J. Silva, H. Frauenrath, W. Craig Carter, F. Stellacci, and S. Guldin, *ChemRxiv* (2021).
- [20] P. Lesiak, K. Bednarska, W. Lewandowski, M. Wójcik, S. Polakiewicz, M. Bagiński, T. Osuch, K. Markowski, K. Orzechowski, M. Makowski, J. Bolek, and T. R. Woliński, *ACS Nano* **13**, 10154–10160 (2019).
- [21] A.L.Rodarte, R.J.Pandolfi, S. Ghosh, and L. Hirst, *J. Mater. Chem. C* **1**, 5527 (2013).
- [22] C.-R. Lee, S.-H. Lin, J.-W. Guo, J.-D. Lin, H.-L. Lin, Y.-C. Zheng, C.-L. Ma, C.-T. Horng, H.-Y. Sun, and S.-Y. Huang, *Optical Materials Express* **5**, 1469 (2015).
- [23] F. Li, J. West, A. Glushchenko, C. I. Cheon, and Y. Reznikov, *Journal of the Society for Information Display* **14**, 523 (2006).
- [24] Z. Tang, X. Zhang, Y. Shu, M. Guo, H. Zhang, and W. Tao, *Nano Today* **36**, 101019 (2021).
- [25] K. H. Basavaraaj, *Indian Journal of Dermatology* **57**, 169 (2012).
- [26] L. Rashidi and K. Khosravi-Darani, *Critical Reviews in Food Science and Nutrition* **51**, 723 (2011).
- [27] P. C. Hohenberg and B. I. Halperin, *Reviews of Modern Physics* **49**, 435,479 (1977).
- [28] E. R. Soulé, C. Lavigne, L. Reven, and A. D. Rey, *Physical Review E* **86**, 011605 (2012).
- [29] A. Matsuyama, *The Journal of Chemical Physics* **128**, 224907 (2008).
- [30] S. Gurevich, E. Soule, A. Rey, L. Reven, and N. Provatas, *Physical Review E* **90**, 020501 (2014).
- [31] F. G. Segura-Fernandez, E. F. Serrato-Garcia, J. E. Flores-Calderon, and O. Guzman, *Frontiers in Physics* **9**, 10.3389/fphy.2021.636288 (2021).
- [32] E. F. Keller and L. A. Segel, *Journal of Theoretical Biology* **26**, 399–415 (1970).
- [33] T. Itahara, H. Tamura, K. Kubota, and T. Uto, *Journal of Nanoscience and Nanotechnology* **15**, 2680 (2015).
- [34] M. Skarabot, Z. Lokar, and I. Musevic, *Physical Review E* **87**, 062501 (2013).
- [35] J. Kołacz, A. Konya, R. L. B. Selinger, and Q.-H. Wei, *Soft Matter* **16**, 1989–1995 (2020).
- [36] S. Samitsu, Y. Takanishi, and J. Yamamoto, *Nature Materials* **9**, 816–820 (2010).
- [37] D. Andrienko, M. Tasinkevych, P. Patricio, and M. M. Telo da Gama, *Physical Review E* **69**, 021706 (2004).
- [38] D. Vollmer, G. Hinze, W. C. K. Poon, J. Cleaver, and M. E. Cates, *Journal of Physics: Condensed Matter* **16**, L227–L233 (2004).
- [39] T. Itahara, H. Tamura, K. Kubota, and T. Uto, *Journal of Nanoscience and Nanotechnology* **15**, 2680–2685 (2015).
- [40] N. Atzin, O. Guzman, O. Gutierrez, L. S. Hirst, and S. Ghosh, *Physical Review E* **97**, 062704 (2018).
- [41] A. DeBenedictis, T. J. Atherton, A. L. Rodarte, and L. S. Hirst, *Phys. Rev. E* **97**, 032701 (2018).
- [42] V. Anderson, E. Terentjev, S. Meeker, J. Crain, and W. Poon, *The European Physical Journal E* **4**, 11–20 (2001).
- [43] M. V. Gorkunov and M. A. Osipov, *Soft Matter* **7**, 4348 (2011).
- [44] A. V. Zakharov and J. Thoen, *The European Physical Journal E* **17**, 447 (2005).
- [45] A. Borštnik, H. Stark, and S. Žumer, *Physical Review E* **61**, 2831 (2000).
- [46] A. V. Ryzhkova and I. Muševič, *Physical Review E* **87**, 032501 (2013).
- [47] H. Stark, *Physics Reports* **351**, 387–474 (2001).
- [48] I. W. Stewart, *The static and dynamic continuum theory of liquid crystals: a mathematical introduction* (Crc Press, 2019).
- [49] M. Cui and J. Kelly, *Molecular Crystals and Liquid Crystals Science and Technology. Section A. Molecular Crystals and Liquid Crystals* **331**, 49 (1999).
- [50] G. Arumugam and J. Tyagi, *Acta Applicandae Mathematicae* **171**, 6 (2021).
- [51] B. M. Shaffer, *The American Naturalist* **91**, 19–35 (1957).
- [52] R. Strehl, *Advanced Numerical Treatment of Chemotaxis-driven PDEs in Mathematical Biology*, Ph.D. thesis, TU Dortmund (2013).
- [53] R. Tyson, L. Stern, and R. J. LeVeque, *Journal of Mathematical Biology* **41**, 455–475 (2000).
- [54] L. J. Khaled-Abad and R. Salehi, *Applied Mathematics and Computation* **409**, 126436 (2021).
- [55] D. Ambrosi, A. Gamba, and G. Serini, *Bulletin of mathematical biology* **66**, 1851 (2004).
- [56] A. Tosin, D. Ambrosi, and L. Preziosi, *Bulletin of mathematical biology* **68**, 1819 (2006).
- [57] R. M. Merks, E. D. Perryn, A. Shirinifard, and J. A. Glazier, *PLoS computational biology* **4**, e1000163 (2008).
- [58] W. K. Ho, L. Freem, D. Zhao, K. J. Painter, T. E. Woolley, E. A. Gaffney, M. J. McGrew, A. Tzika, M. C. Milinkovitch, P. Schneider, *et al.*, *PLoS Biology* **17**, e3000132 (2019).
- [59] A. Bray, *Advances in Physics* **43**, 357–459 (1994).
- [60] V. Popa-Nita and T. J. Sluckin, *Journal de Physique II* **6**, 873–884 (1996).
- [61] S. Riahinassab, A. Elbaradei, A. Keshavarz, B. Stokes, and L. Hirst, *Proc. of SPIE* **10125**, 1012503 (2017).